GEOPHYSICS, VOL. 72, NO. 2 (MARCH-APRIL 2007); P. C31–C43, 12 FIGS., 5 TABLES.
10.1190/1.2435604

AVO inversion of BSRs in marine gas hydrate studies

Marc-André P. Chen[1], Michael Riedel[2], Roy D. Hyndman[1], and Stan E. Dosso[3]

ABSTRACT

We examine the usefulness of amplitude versus offset (AVO) analysis of bottom-simulating reflections (BSRs) for estimating associated marine gas hydrate and free-gas concentrations. A nonlinear Bayesian inversion is applied to estimate marginal probability distributions (MPDs) of physical parameters at a BSR interface, which are related to overlying gas hydrate and underlying free-gas concentrations via rock physics modeling. The problem is constrained further by prior information and re-parameterization of inversion results. Inversion of BSR AVO data from offshore Vancouver Island, Canada, shows that gas hydrate and free-gas concentrations are, respectively, 0%–23% and 0%–2% of the pore volume, at a 90% credibility level. This result indicates that the data do not provide sufficient information to independently resolve gas hydrate and free-gas concentrations to useful accuracy. The study is directed primarily at AVO for gas-hydrate-related BSRs, but may have important applicability in testing the degree of constraint of formation characteristics in other AVO studies. The inversion method is applied also to synthetic AVO data generated from Ostrander's gas-sand model. In this case, MPDs sufficiently constrain the relationship between P- and S-wave velocities in the sandstone unit to determine if it is gas-charged. The variable degree of model constraint obtained in this AVO study highlights the need to include rigorous quantitative uncertainty analysis in all AVO studies.

INTRODUCTION

Gas hydrate is a solid substance consisting of a water lattice in which hydrocarbon molecules (most often methane) are embedded. Marine gas hydrate occurs in the top few hundred meters of sediments on the continental slope, and can substantially increase the sediment seismic velocity. Their presence is usually inferred from a prominent bottom-simulating reflection (BSR) on low-frequency seismic sections, that marks the base of the gas hydrate stability field (e.g., Hyndman and Spence, 1992; Yuan et al., 1996; Andreassen et al., 1997). BSRs are observed in reflection seismic data from continental margins worldwide, especially in subduction accretionary prisms (Kvenvolden et al., 1993). They occur as negative polarity reflections, indicating a decrease in acoustic impedance, which is consistent with a transition in sediment pore-space saturation from gas hydrate above to free-gas below the boundary.

In the well-studied gas hydrate area in the northern Cascadia accretionary prism, offshore Vancouver Island, Canada, a widespread BSR is observed throughout the mid portion of the continental slope, and has been shown to be caused by gas hydrate and free gas by Ocean Drilling Program (ODP) Leg 146 (Westbrook et al., 1993) and Integrated Ocean Drilling Program (IODP) Expedition 311 (Collett et al., 2005). Although BSRs in Northern Cascadia can be related confidently to gas hydrate occurrence, there has been little success in relating BSR amplitude and character (and other information from regional seismic surveys) to quantitative estimates of gas hydrate and free-gas concentrations.

The successful use of seismic amplitude versus offset (AVO) studies as hydrocarbon indicators in the oil and gas industry has prompted the scientific community to use AVO as a tool in gas hydrate-related BSR studies (Hyndman and Spence, 1992; Andreassen et al., 1997; Ecker et al., 1998; Yuan et al., 1999). AVO data can be gathered from multichannel streamer data, and provide information about the sediment density and its compressional- (P-) wave and shear- (S-) wave velocity. The occurrence of gas hydrate in sediment pore space should increase both P- and S-wave velocities above the

Manuscript received by the Editor May 10, 2006; revised manuscript received September 21, 2006; published online March 1, 2007.
[1]University of Victoria, School of Earth and Ocean Sciences, Victoria, British Columbia, Canada and Pacific Geoscience Centre, Sidney, British Columbia, Canada. E-mail: mchen@uvic.ca; rhyndman@nrcan.gc.ca.
[2]McGill University, Department of Earth and Planetary Sciences, Montreal, Quebec, Canada. E-mail: mriedel@eps.mcgill.ca.
[3]University of Victoria, School of Earth and Ocean Sciences, Victoria, British Columbia, Canada. E-mail: sdosso@uvic.ca.

BSR (e.g., Dvorkin and Nur, 1993; Helgerud, 2001). Below the BSR, the occurrence of free gas should significantly reduce P-wave velocities (Gregory, 1976), although not greatly influencing S-wave velocities (relative to a no-gas reference). Changes in both P- and S-wave velocities should therefore occur across the BSR, making gas hydrate studies a potential candidate for AVO analysis.

The common approach in gas hydrate AVO studies has been to estimate gas hydrate and free-gas concentrations immediately above and below the BSR by matching the measured AVO response of the BSR to synthetic AVO curves for different gas hydrate/free-gas concentration scenarios and rock physics models (Andreassen et al., 1997; Ecker et al., 1998; Yuan et al., 1999). However, forward modeling schemes do not rigorously consider the uncertainties of the AVO problem related to the nonunique nature of the solution and the uncertainty in the AVO data. The large uncertainties caused by nonuniqueness of AVO solutions were recognized by Yuan et al. (1999), who studied the AVO response of BSRs in Northern Cascadia through forward modeling. They found that scenarios with high gas hydrate concentration above the BSR and low free-gas concentration below could not be distinguished from scenarios with low gas hydrate concentration above the BSR and high free-gas concentration below. This finding highlights the need to include quantitative uncertainty analysis in AVO studies. To achieve this, an amplitude-preserving data processing scheme must be implemented, data uncertainties (such as measurement of reflection coefficients and incidence angles) need to be estimated quantitatively, and the inversion approach must explore fully the solution space of the problem (i.e., the ensemble of all possible solutions).

This study determines to what extent AVO data from BSRs can be used to estimate associated gas hydrate and free-gas concentrations. To this end, a nonlinear Bayesian inversion is applied to BSR AVO data to obtain estimates and uncertainties of formation physical parameters (P- and S-wave velocities and densities), which are then used to estimate gas hydrate and free-gas concentrations. The Bayesian approach treats model parameters as random variables, giving their estimates in terms of probability distributions (Sen and Stoffa, 1996; Riedel et al., 2003), thus quantifying model uncertainties. Gas-hydrate and free-gas concentration estimates apply to the sediments immediately above and below the BSR. The vertical resolution of the estimates depends on the seismic wavelength, which is ~ 50 m at BSR depths for the data used in this study.

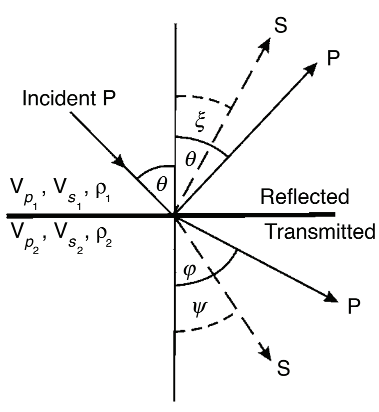

Figure 1. Schematic ray diagram of the partitioning of an incident P-wave into reflected and transmitted P- and converted S-waves at a half-space/half-space interface.

This paper examines a set of synthetic test cases that emulates multichannel seismic (MCS) data with a strong BSR to assess the potential for successful AVO inversion of BSR data. Prior knowledge of physical parameters, including theoretical or empirical relationships, is used to further constrain the problem. The inversion is applied to BSR AVO data from offshore Vancouver Island to provide quantitative estimates of the range of gas hydrate and free-gas concentrations immediately above and below the BSR. Finally, as a reference test, the inversion is applied to synthetic data from the now-classic Ostrander (1984) gas-sand model, and the results are compared to those of the BSR study.

THEORY

Zoeppritz equations

AVO theory is based on the Zoeppritz (1919) equations, expressing the reflection and transmission coefficients of a plane wave incident on a planar interface between two homogeneous media as a function of the angle of incidence and the elastic properties of the media (Figure 1). Of interest in MCS studies are P-to-P reflections, described in terms of the reflection coefficient R:

$$R = \left[\left(b\frac{\cos\theta}{Vp_1} - c\frac{\cos\varphi}{Vp_2} \right) F - \left(a + d\frac{\cos\theta}{Vp_1}\frac{\cos\psi}{Vs_2} \right) Hp^2 \right] \Big/ D, \qquad (1)$$

with

$$a = \rho_2(1 - 2Vs_2^2p^2) - \rho_1(1 - 2Vs_1^2p^2), \quad b = \rho_2(1 - 2Vs_2^2p^2) + 2\rho_1 Vs_1^2p^2,$$
$$c = \rho_1(1 - 2Vs_1^2p^2) + 2\rho_2 Vs_2^2p^2, \quad d = 2(\rho_2 Vs_2^2 - \rho_1 Vs_1^2),$$
$$E = b\frac{\cos\theta}{Vp_1} + c\frac{\cos\varphi}{Vp_2}, \quad F = b\frac{\cos\zeta}{Vs_1} + c\frac{\cos\psi}{Vs_2},$$
$$G = a - d\frac{\cos\theta}{Vp_1}\frac{\cos\psi}{Vs_2}, \quad H = a - d\frac{\cos\varphi}{Vp_2}\frac{\cos\zeta}{Vs_1},$$
$$D = EF + GHp^2,$$

where Vp, Vs, and ρ are, respectively, P-wave velocity, S-wave velocity, and bulk density (with subscripts 1 and 2 indicating the upper and lower media). The incidence angle is θ, ϕ and ψ are the P-wave and converted S-wave transmission angles, and ξ is the S-wave reflection angle related by Snell's law:

$$p = \frac{\sin\theta}{Vp_1} = \frac{\sin\varphi}{Vp_2} = \frac{\sin\zeta}{Vs_1} = \frac{\sin\psi}{Vs_2}, \qquad (2)$$

where p is the ray parameter.

Bayesian inversion

Bayesian methods can be applied to geophysical inverse problems to provide quantitative uncertainty estimates and can include constraints from prior information (Tarantola, 1987; Sen and Stoffa, 1996). The method used in this study follows the approach of Riedel et al. (2003), who inverted seafloor AVO data for seabed properties.

Consider a vector of N-observed AVO data $\mathbf{R}^{\mathrm{obs}}$ (i.e., P-wave reflection coefficients at the N angles of incidence), related to a model $\mathbf{m} = [Vp_1, Vs_1, \rho_1, Vp_2, Vs_2, \rho_2]^T$ of physical parameters by a function $\mathbf{R}^{\mathrm{obs}} = \mathbf{R}(\mathbf{m}) + \mathbf{n}$, where $\mathbf{R}$ represents the Zoeppritz equations. For Gaussian-distributed errors $\mathbf{n}$ with data covariance matrix $\mathbf{C_D}$, the likelihood function is

$$L(\mathbf{R}^{\text{obs}}|\mathbf{m}) = \frac{1}{(2\pi)^{N/2}|\mathbf{C_D}|^{1/2}} \times \exp\left\{-\frac{1}{2}[\mathbf{R}(\mathbf{m}) - \mathbf{R}^{\text{obs}}]^T \times \mathbf{C_D}^{-1}[\mathbf{R}(\mathbf{m}) - \mathbf{R}^{\text{obs}}]\right\}. \quad (3)$$

In Bayesian inversion, the data and model vectors are considered random variables that obey Bayes' rule, which can be written as

$$P(\mathbf{m}|\mathbf{R}^{\text{obs}}) \propto L(\mathbf{R}^{\text{obs}}|\mathbf{m})P(\mathbf{m}), \quad (4)$$

where $P(\mathbf{m}|\mathbf{R}^{\text{obs}})$ represents the posterior probability distribution (PPD) and $P(\mathbf{m})$ is the prior distribution representing any available information about the model parameters that is known independently of the data (Tarantola, 1987). For likelihood $L(\mathbf{R}^{\text{obs}}|\mathbf{m}) \propto \exp[-E(\mathbf{m})]$, where the error function $E(\mathbf{m})$ is the argument of the exponential function in equation 3, the normalized PPD may be written as

$$P(\mathbf{m}|\mathbf{R}^{\text{obs}}) = \frac{\exp[-\lambda(\mathbf{m})]}{\int \exp[-\lambda(\mathbf{m}')]d\mathbf{m}'}, \quad (5)$$

where $\lambda(\mathbf{m}) = E(\mathbf{m}) - \ln P(\mathbf{m})$, and the domain of integration spans the model space.

From a Bayesian viewpoint, $P(\mathbf{m}|\mathbf{R}^{\text{obs}})$ is the general solution of the inverse problem; however, interpretation of the PPD for multidimensional problems requires the computation of integral properties (moments) of the distribution. In particular, the marginal probability distribution (MPD) of parameter m_i provides a 1D uncertainty distribution by integrating over all other parameters:

$$P(m_i|\mathbf{R}^{\text{obs}}) = \int \delta(m_i' - m_i)P(\mathbf{m}'|\mathbf{R}^{\text{obs}})d\mathbf{m}', \quad (6)$$

where δ is the Dirac delta function. Two-dimensional (joint) MPDs illustrate interrelationships between parameters and are defined similarly to equation 6. MPDs can be used also to calculate highest probability density credibility intervals: the smallest interval in the model space containing a given percentage of the total probability. To solve the integral of equation 6 for nonlinear problems, a Metropolis Gibbs' sampling approach is used (Dosso, 2002; Riedel et al., 2003).

Bayesian inversion requires an estimate of the data covariance matrix $\mathbf{C_D}$, including both measurement and theory errors. Here, $\mathbf{C_D}$ is assumed to be of the form

$$\mathbf{C_D} = \hat{\sigma}^2\mathbf{I} + \mathbf{C_0}, \quad (7)$$

where $\hat{\sigma}$ is the standard deviation of the uncorrelated component of the data errors, and $\mathbf{C}_0$ represents correlated errors arising from the data processing (discussed later, in "Data and processing"). The maximum-likelihood estimate for $\hat{\sigma}$ is given by

$$\hat{\sigma}^2 = \frac{1}{N-M}|\mathbf{R}(\hat{\mathbf{m}}) - \mathbf{R}^{\text{obs}}|^2, \quad (8)$$

where M is the number of model parameters, and $\hat{\mathbf{m}}$ is the maximum-likelihood model estimate, determined here using a hybrid optimization algorithm (Dosso et al., 2001).

SYNTHETIC STUDIES

Model design

To assess the reliability of AVO analysis in marine gas hydrate studies, synthetic test cases typical of AVO data for BSRs are considered. The model consists of a planar interface between two half-spaces, with model parameters Vp_1, Vs_1, ρ_1, Vp_2, Vs_2, and ρ_2 (Figure 1). The interface represents the base of the gas hydrate stability field, with model parameters representative of realistic gas hydrate/free-gas concentration scenarios. P- and S-wave velocities for both media are based on the gas hydrate in-frame rock physics model of Helgerud (2001) for gas hydrate and free-gas concentrations in the upper and lower media, respectively. The rock physics model is an effective medium theory that considers the gas hydrate to be a component of the load-bearing sediment matrix without grain cementation. The model predicts that gas hydrate increases both P- and S-wave velocity, but less than a gas hydrate cementation model (e.g., Dvorkin and Nur, 1993). The gas hydrate in-frame model is supported by downhole VSP data from ODP Leg 164 hole 995 at the Blake-Bahama Ridge gas hydrate site (Helgerud, 2001). A key feature of the rock physics model is that, although Vs in the upper medium is sensitive to gas hydrate occurrence, it is nearly unaffected in the lower medium by the presence of free gas in the pore space because the replacement of brine with gas does not affect the sediment shear modulus (Gassmann, 1951). At higher gas concentrations, the fluid density change can significantly affect the S-wave velocity; however, this is not a concern here, with free-gas concentrations on the order of 1% of the pore space. Also, the base of the gas hydrate stability field does not coincide with a lithologic boundary (Westbrook et al., 1993), so the physical parameter values derived from the rock physics model in the upper and lower media are calculated for sediments of identical lithology. The densities chosen for the model are consistent with downhole well-log measurements from ODP Leg 146 (Westbrook et al., 1993), Leg 204 (Tréhu et al., 2003), and IODP Expedition 311 (Collett et al., 2005), and reflect the increase of density with depth caused by porosity loss (~50% porosity at BSR depths) related to sediment compaction (e.g., Hamilton, 1976). Table 1 summarizes the physical parameters adopted for the true model for a scenario with 15% gas hydrate concentration (defined here as the volume fraction of the pore space occupied by gas hydrate) above the BSR and 1% free-gas concentration below. These choices of gas hydrate and free-gas concentrations give values for Vp_1 and Vp_2 in agreement with velocities from NMO analysis in Northern Cascadia (Yuan et al., 1996).

Synthetic AVO data are generated from the true model parameters using the Zoeppritz equations (equation 1), with data noise level and angular range that emulate typical AVO data. Two synthetic AVO data sets for the true model are generated (Figure 2) that have angular ranges of 0°–80° and include random independent Gaussian-distributed errors of 0.01 and 0.05 standard deviation. These data represent the case $Vp_1 > Vp_2$, giving negative reflection coefficients and

Table 1. Physical parameters adopted for the 15% gas hydrate/1% free-gas model.

	Vp (m/s)	Vs (m/s)	ρ (kg/m^3)
Upper medium	1768	421	1800
Lower medium	1481	350	1850

no critical angle. The synthetic AVO data are inverted, using the Bayesian approach, to determine uncertainties in physical parameters and in gas hydrate and free-gas concentrations. Table 2 summarizes all the synthetic cases considered in this section.

Factors for successful AVO inversion

To determine the most important factors affecting the uncertainty in AVO, this study begins with a scenario that provides well-constrained results. The synthetic AVO curve for this scenario (referred to as case 1a) represents a best-case for data quality, in terms of angular range and data-noise level. From the synthetic AVO curve, parameter estimates and uncertainties are computed using the Bayesian inversion approach, for the case of known upper medium parameters and wide uniform bounds for the lower medium (parameter bounds are summarized in Table 3). The resulting MPDs are shown in Figure 3 (case 1a), represented by histograms normalized so that the integral over the parameter bounds is unity. In this case, Vp_2, Vs_2, and ρ_2 are well constrained by the inversion. This is analogous to the successful AVO inversion for physical parameters of seabed sediments achieved by Riedel et al. (2003), where the upper medium is the water column, with well-known physical properties.

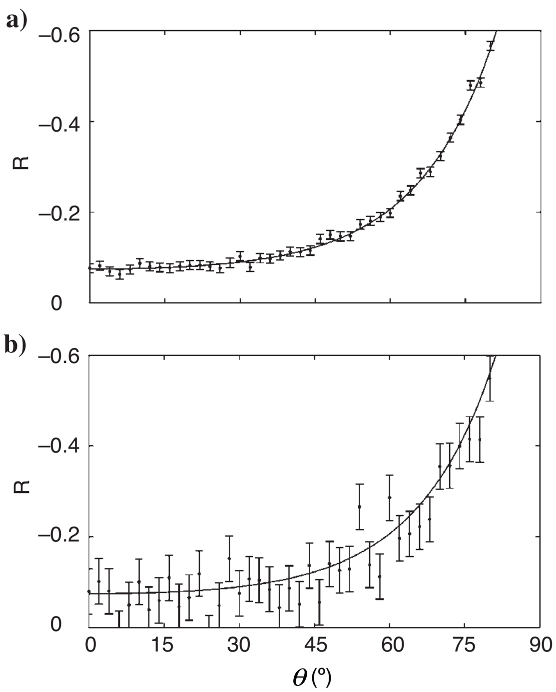

Figure 2. Synthetic AVO data with varying amounts of random Gaussian noise. In (a), $\sigma = 0.01$; and (b), $\sigma = 0.05$. One-standard-deviation error bars are shown and the solid line is the error-free AVO curve. These AVO data are generated from the true model summarized in Table 1.

Table 2. Summary of all models in the synthetic studies section.

	Model 1: Factors for a successful AVO inversion	Model 2: Inversion with additional constraints
Case a	Reference model	No prior information
Case b	Increased data-noise level	Density constraints
Case c	Decreased angular range	V_p–V_s relation constraints
Case d	Unknown upper parameters	P-wave velocity constraints

Data of this quality and angular range are seldom available from MCS surveys, and the physical parameters of the upper medium are usually poorly known. To determine the effect of each of these factors independently, three additional synthetic cases are tested. In case 1b, the standard deviation of the errors on the synthetic data is increased from 0.01 to 0.05 (Figure 2b); in case 1c, the range of incidence angles is reduced from 0°–80° to 0°–40°; and in case 1d, physical parameters for both media are considered unknown. Cases 1a–d are summarized in Table 3, and inversion results are shown as MPDs in Figure 3. These distributions indicate that the factors affecting the uncertainty in inversion results are, in order of importance, (1) the number of unknown parameters, (2) the range of incidence angles, and (3) the data noise level.

Inversion with additional constraints

Prior information and reparameterization

This section considers a second set of synthetic test cases using the data from Figure 2a to investigate the improvement in parameter resolution that can be achieved using prior information in the form of narrow parameter bounds or specified parameter interrelationships. Reparameterizations of the results are also applied, recognizing that the goal of this analysis is not to determine individual model parameters, but rather to determine gas hydrate and free-gas concentrations. Inversion results are reparameterized in terms of (1) the fractional change in P-wave velocity $\Delta Vp/Vp$, (2) the fractional change in S-wave velocity $\Delta Vs/Vs$, and (3) the squared S- to P-wave velocity ratio $(Vs/Vp)^2$, where Δ represents the difference between the lower and upper media, and Vp, Vs, or ρ without a subscript indicates the mean value of the two media. For the purposes of this paper, these new parameters are referred to as parameter combinations, and $\Delta Vp/Vp$ and $\Delta Vs/Vs$ are referred to as P- and S-wave reflectivity. This parameterization is useful for AVO analysis because it highlights relationships between the original parameters that are typically well resolved by reflection seismic data (i.e., seismic reflections provide more information about the change in physical parameters across the interface than about the parameters themselves).

In case 2a, the parameters of both media are unknown: The inversion is computed using uniform bounds on all parameters, wider than those expected for unconsolidated sediments. In case 2b, tighter prior bounds are applied to the density of both media. Uniform prior bounds for ρ_1 and ρ_2 at the BSR are set to be 1800 ± 100 and 1850 ± 100 kg/m^3, respectively (the occurrence of gas hydrate or free gas in relatively low concentration has little effect on bulk density). The requirement $\rho_1 \leq \rho_2$ is also imposed, forcing an increase in density with depth, related to porosity loss and sediment compaction (e.g., Hamilton, 1976). In case 2c, a further constraint is imposed in which Vs_1 is related to Vp_1 through a linear relationship, based on the gas hydrate in-frame rock physics model given by Helgerud (2001), with deviations from this trend of no more than ± 200 m/s allowed for Vs_1:

$$Vs_1 = (0.4004Vp_1 - 292) \pm 200. \quad (9)$$

This relationship is similar to the mudrock relation of Castagna et al. (1985), within the range of expected values. Case 2d also includes constraints on P-wave velocities from a hypothetical normal moveout (NMO) velocity analysis. Uncertainties in NMO velocities are estimated by Yuan et al. (1994) to be ±5% for carefully determined interval velocities, corresponding approximately to ±100 m/s at BSR depths. Conservative uncertainty estimates of ±150 and ±200 m/s for Vp_1 and Vp_2 are used as uniform prior bounds with respect to true model values. The wider bounds for Vp_2 reflect the greater uncertainty in NMO velocities in the free-gas zone beneath the BSR. MPDs and joint MPDs for the inverted physical parameters and parameter combinations of cases 2a–d are displayed in Figures 4-6, and Table 4 provides a summary of all cases.

Inversion Results

The MPDs for case 2a show that individual model parameters cannot be resolved if wide parameter bounds are used without additional prior information (Figure 4a). However, joint MPDs (Figure 5a) show strong positive correlations between both Vp_1 and Vp_2, and Vs_1 and Vs_2 (correlation coefficients of 0.995 and 0.986). The correlation between P-wave velocities is a result of the data accurately resolving the P-wave impedance contrast. P-wave velocities (and densities) across the boundary must vary in a specific way to fit the AVO data. A similar argument holds for the correlation between Vs_1 and Vs_2. These two interparameter correlations ($Vp_1 - Vp_2$ and $Vs_1 - Vs_2$) are tightly constrained in terms of the parameter combinations (Figure 6a), and MPDs indicate that the P-wave reflectivity is well constrained, but the S-wave reflectivity is underestimated.

In case 2b, with prior density constraints, MPDs and joint MPDs of all parameters are nearly identical to those of case 2a (Figures 4-6), with the exception of density MPDs. This indicates that the additional density constraints do not provide significant information about the other parameters.

To improve S-wave reflectivity resolution, case 2c includes a constraint that relates S-wave velocity to P-wave velocity in the upper media (equation 9). MPDs of individual model parameters (Figure 4c) are still too wide to resolve individual parameter values, whereas joint MPDs (Figure 5c) show strong positive correlations between Vp_1 and Vp_2, and Vs_1 and Vs_2 (correlation coefficients of 0.997 and 0.977). The observed correlation between Vp_1 and Vs_1 (correlation coefficient of 0.877) is a result of the prior relationship imposed on these parameters, which in turn forces a weaker correlation between Vp_2 and Vs_2. MPDs of the parameter combinations show well-constrained distributions for P- and S-wave reflectivity (Figure 6c) because of strong correlations between the physical parameters. The S-wave reflectivity is less well resolved than the P-wave reflectivity, but it is no longer skewed toward zero. MPDs of the parameter combinations also show that $(Vs/Vp)^2$ remains poorly resolved. This demonstrates that the data provide more information about P-wave velocity contrasts than S-wave velocity contrasts, and almost no information about the relation between S- and P-wave velocities. The inversion was tested also using narrower bounds on equation 9, but results were not improved significantly.

In case 2d, prior information is added to Vp_1 and Vp_2 by limiting P-wave velocity bounds, based on estimated uncertainties obtained hypothetically from NMO velocity analysis. By including this additional prior information in the inversion, the MPDs for Vp_1 and Vp_2 are constrained better than in previous cases. However, Figure 4d shows that the MPDs are essentially unconstrained by the data because these distributions are approximately flat within these prior bounds. This suggests that, for determining P-wave velocities, AVO is not as informative as NMO velocity analysis. For MPDs of the parameter combinations, the effect of the additional P-wave velocity constraints on the resolution of the interparameter relationships is negligible (Figure 6d).

The results clearly show the inability of the data to provide information about the Vp–Vs relationship in each medium (Figure 5a-d). This greatly limits the ability of AVO to independently constrain gas hydrate and free-gas concentrations. In all cases, the best-resolved parameter (P-wave reflectivity) depends on Vp_1 and Vp_2, so its value does not depend uniquely on gas hydrate or free-gas concentration. However, the parameter interrelationships observed in Figure 5 justify the choice of P-wave reflectivity, S-wave reflectivity, and $(Vs/Vp)^2$ as an appropriate reparameterization because they highlight the strongest correlations observed between individual parameters.

Of the four cases tested, case 2d exhibits the most tightly constrained distributions (Figure 6d) because it includes the most prior information. Of the individual MPDs of case 2d, S- and P-wave reflectivity are the best-constrained parameters and, therefore, should provide the most information on gas hydrate and free-gas concentrations. A joint MPD of these parameters is shown in Figure 7 as a contour plot, with individual contours indicating different credibility levels. The MPD is overlain with a grid indicating S- and P-wave reflectivity values for various gas hydrate and free-gas concentrations. The grid values are calculated from the gas hydrate in-frame rock

Table 3. True model physical parameters for a 15% gas hydrate/1% free-gas model, prior bounds, angular range, and data quality used for cases 1a–d. The specific modification of each case from case 1a is shown in bold.

Parameter	Vp_1 (m/s)	Vs_1 (m/s)	ρ_1 (kg/m^3)	Vp_2 (m/s)	Vs_2 (m/s)	ρ_2 (kg/m^3)	Angular range (°)	σ data err.
True value	1768	421	1800	1481	350	1850	-	-
Case 1a	-	-	-	-	-	-	0–80	0.01
Lower bound	-	-	-	10	10	1000	-	-
Upper bound	-	-	-	3000	2000	2500	-	-
Case 1b	-	-	-	-	-	-	0–80	**0.05**
Lower bound	-	-	-	10	10	1000	-	-
Upper bound	-	-	-	3000	2000	2500	-	-
Case 1c	-	-	-	-	-	-	**0–40**	0.01
Lower bound	-	-	-	10	10	1000	-	-
Upper bound	-	-	-	3000	2000	2500	-	-
Case 1d	-	-	-	-	-	-	0–80	0.01
Lower bound	**1000**	**10**	**1000**	10	10	1000	-	-
Upper bound	**3000**	**2000**	**2500**	3000	2000	2500	-	-

physics model (Helgerud, 2001) by forward modeling. Parameters Vp_1, Vs_1, Vp_2, and Vs_2 are calculated for different gas hydrate and free-gas concentrations, and are then used to compute P- and S-reflectivity. The grid translates inversion results, given in terms of physical parameters, into gas hydrate and free-gas concentrations via rock physics modeling. The intersection of the grid with a given credibility level contour of the MPD provides a quantitative range of gas hydrate/free-gas concentration scenarios that are consistent with the synthetic AVO data and the prior information for case 2d. For example, both a 0% gas hydrate/3% free-gas scenario and a 25% gas hydrate/0% free-gas scenario satisfy the AVO data to a 90% credibility level. The poor S-wave reflectivity resolution does not allow high gas hydrate/low free-gas concentration scenarios to be distinguished from low gas hydrate/high free-gas concentration scenarios.

Inversion of synthetic AVO data for a true model with 25% gas hydrate and 2% free gas was also tested, and similar poorly constrained results were obtained.

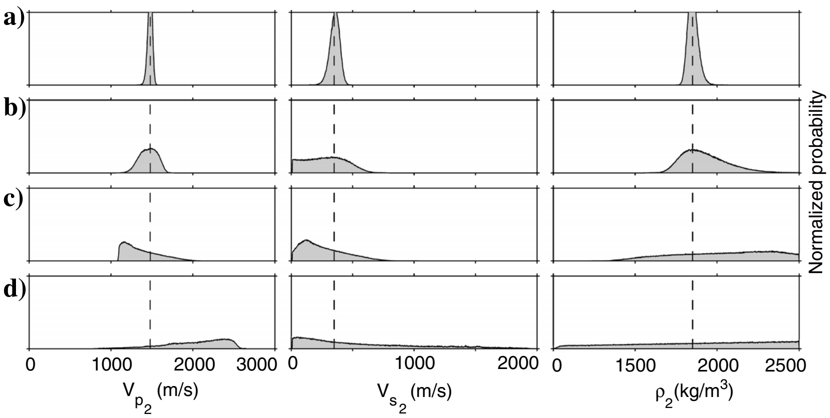

Figure 3. MPDs for parameters of the lower medium from synthetic cases 1a–d, normalized so that the area of each distribution is unity. Dashed lines indicate the true parameter values. (a) Case 1a, the reference model; (b) case 1b, with $\sigma = 0.05$; (c) case 1c, with angular range of 0°–40°; and (d) case 1d, with parameters of the upper medium unknown.

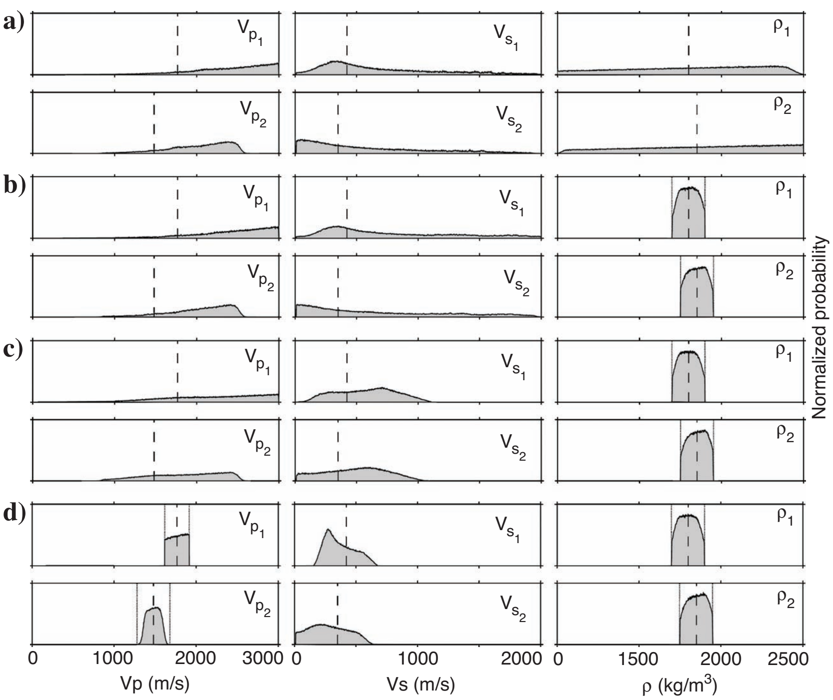

Figure 4. MPDs for parameters of the upper and lower media from synthetic cases 2a–d, normalized so that the area of each distribution is unity. Dashed lines indicate the true parameter values and dotted lines indicate the prior bounds used in the inversion. (a) Case 2a, with no additional prior information; (b) case 2b, with prior constraints on density; (c) case 2c, with prior constraints on density and the $Vp_1 - Vs_1$ relation; and (d) case 2d, with prior constraints on density, the $Vp_1 - Vs_1$ relation, and P-wave velocity.

INVERSION OF NORTHERN CASCADIA DATA

Data and processing

This section considers AVO data from an MCS line in Northern Cascadia, offshore Vancouver Island. The seismic data are discussed by Spence et al. (1991a, b). The location chosen for the AVO inversion is on the midcontinental slope, where a prominent BSR is present. Because the MCS line (line 89-08) is in the dip direction, a location with relatively flat topography and apparent horizontal subsurface structure is chosen to avoid complications resulting from dipping reflectors. The location is close to ODP site 889/890 (Leg 146) and IODP site U1327 (Expedition 311), where the base of the gas hydrate stability zone occurs at 225 m depth (Westbrook et al., 1993; Collett et al., 2005), and reliable P-wave velocity and density information are available from well logs.

The MCS survey was collected by Digicon Geophysical Corporation in 1989, using a DSS-240 recording system. The air-gun source was a tuned array with a total volume of 125 L (7820 inch^3). Shots were recorded by a 3600-m streamer with 144 hydrophones, with minimum and maximum offsets of 183 and 3783 m from the source, for a group interval of 25 m. The shotpoint interval was 50 m, giving CDPs with 36-fold multiplicity. The record length was 14 s at a 4-ms sampling interval. A stacked section of the area of interest and super CDP gather of data used in the inversion are shown in Figure 8.

The MCS survey provided amplitude data as a function of source-receiver offset. For quantitative AVO analysis, BSR reflection coefficients as a function of BSR incidence angles are required. True BSR incidence angles were obtained from source-receiver offsets by ray tracing through a 1D velocity model derived from semblance velocity analysis. At the maximum offset of 3783 m, in 1300 m water depth, the incidence angle at the seafloor was 49° and increased to 67° at the BSR (225 m below the seafloor) because of increasing velocity with depth. The calculation of angle-dependent reflection coefficients required a true-amplitude data processing scheme (e.g., Duren, 1991). The processing is divided into time- and offset-dependent corrections. The time-dependent corrections to be considered are for geometric spreading and attenuation. Simplified geometric spreading corrections were obtained by multiplying arrival amplitudes by their arrival traveltimes. Because the BSR is at such a shallow depth below the seafloor, this correction is a good approximation for the BSR as well as the seafloor reflection. Because of the shallow depth of the BSR and the short travel path through sediment, corrections for attenuation are unnecessary, given attenuation estimates in marine gas hydrate-bearing sediments (Wood et al., 2000).

For offset dependent corrections, previous work on this MCS survey (Hyndman and Spence, 1992; Yuan et al., 1999) used corrections for source and receiver directivity based on hydrophone array attenuation as a function of incidence angle (Sheriff and Geldart,

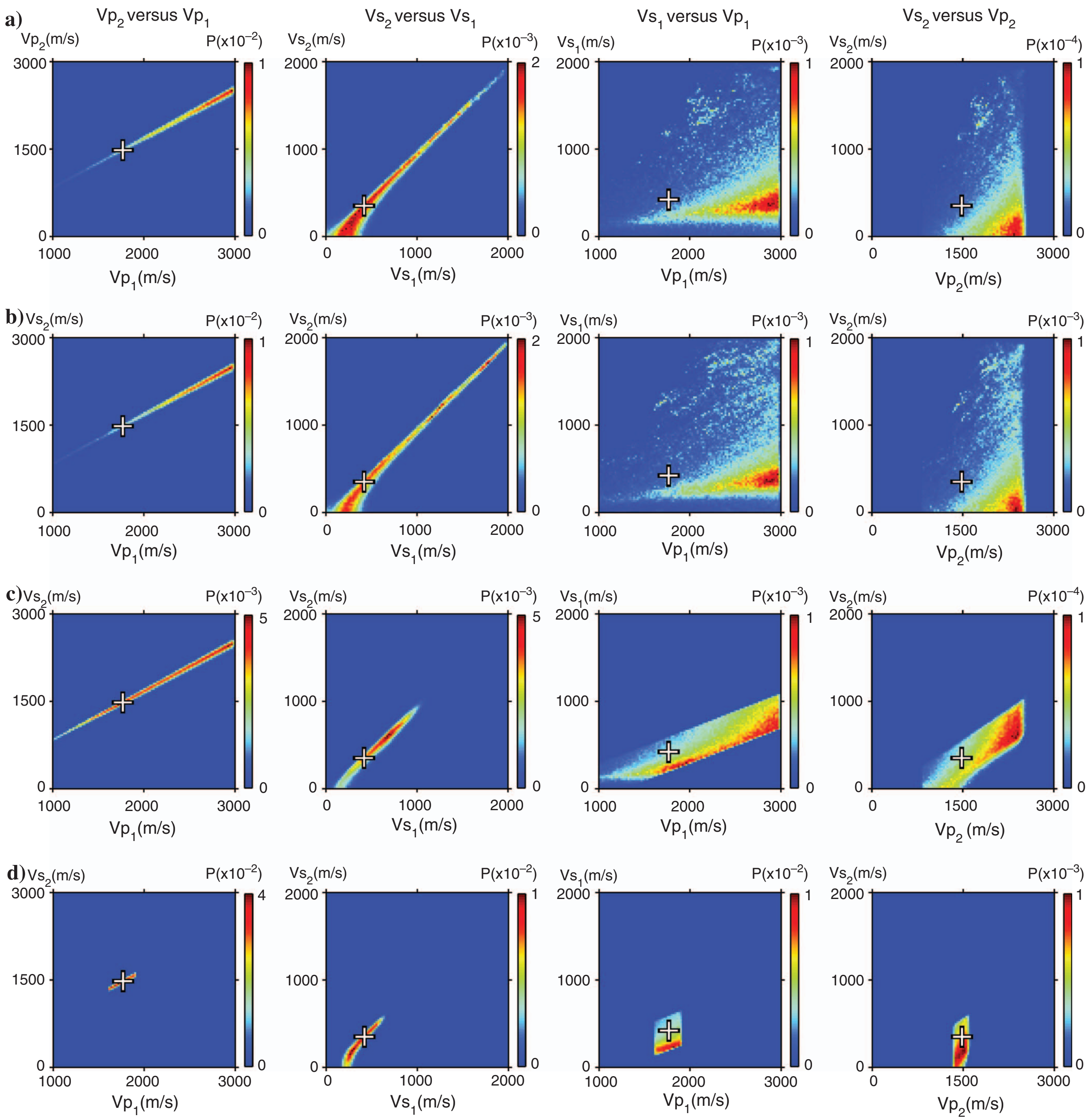

Figure 5. Joint MPDs of selected parameters from synthetic cases 2a-d. The colorbar scale is normalized probability (P) and the cross indicates the true parameter values. (a) Case 2a, with no additional prior information; (b) case 2b, with prior constraints on density; (c) case 2c, with prior constraints on density and the $Vp_1 - Vs_1$ relation; and (d) case 2d, with prior constraints on density, the $Vp_1 - Vs_1$ relation, and P-wave velocity.

1982), and source waveform as a function of outgoing angle provided by Digicon Geophysical Corporation. Because of the difficulty in quantifying the uncertainty in these corrections (especially the source waveform function), the approach taken here is to account for all offset-dependent corrections by calibration of the measured seafloor AVO to the seafloor AVO expected for a realistic model of the seafloor, based on ODP drilling results (Westbrook et al., 1993; Collett et al., 2005) and seismic NMO analyses (see Andreassen et al., 1995, who used the same method). This is an empirical approach to derive an offset-dependent correction that combines all of the uncertainties resulting from source/receiver directivity and variable seafloor characteristics via trace normalization. However, rather than utilizing a single value for each of the seafloor physical parameters, the method is extended by using a range of values to quantify the uncertainty of the offset-dependent correction.

A Monte Carlo simulation is carried out, where a large sample of expected seafloor AVO curves is generated from the Zoeppritz equations (equation 1), by randomly choosing seabed parameters from Gaussian probability distributions representing the best estimates of the expected value and standard deviation for Vp_{sf}, Vs_{sf}, and ρ_{sf} of 1570 ± 20 m/s, 170 ± 40 m/s, and 1760 ± 50 kg/m^3, respectively. Fixed values of 1460 m/s and 1020 kg/m^3 are used for seawater velocity and density. Each seafloor AVO curve R_{sf} of the Monte Carlo sample is used to compute a BSR AVO curve R_{bsr}, which accounts for offset-dependent corrections, given expected seafloor AVO for that particular trial of the Monte Carlo simulation:

$$R_{bsr} = \frac{A_{bsr}}{A_{sf}} R_{sf}(1 - R_{sf}^2)^{-1}. \quad (10)$$

A_{sf} and A_{bsr} are seafloor and BSR amplitudes after time-dependent corrections, chosen as the peak signal level for a given reflection, measured prior to NMO, and averaged at each angle (offset) over four adjacent CDPs to improve the S/N. After time-dependent corrections, the ratio A_{bsr}/A_{sf} remains fixed at a given angle, so the offset-dependent corrections are achieved in equation 10 by scaling the amplitude ratio in a given trace by a factor of $R_{sf}(1 - R_{sf}^2)^{-1}$, where R_{sf} depends on the realization of the Monte Carlo simulation. The factor $(1 - R_{sf}^2)^{-1}$ accounts for transmission loss at the seafloor (Yuan et al., 1999).

The BSR AVO data used in the inversion (Figure 9a) are calculated, at each trace, as the sample mean of R_{bsr} over the Monte Carlo simulation, for that trace. The R_{bsr} data are used then to compute a covariance matrix representing the uncertainty in directivity corrections:

$$\mathbf{C_0} = \langle (\mathbf{r} - \langle \mathbf{r} \rangle)(\mathbf{r} - \langle \mathbf{r} \rangle)^T \rangle, \quad (11)$$

where $\mathbf{r}$ is a vector of the BSR AVO data R_{bsr} for a given realization of the Monte Carlo simulation.

The complete data covariance matrix $\mathbf{C_D}$, which considers both measurement errors and uncertainties in the directivity correction, is obtained via equation 7, and is shown in Figure 9b. The independent, identically distributed component of the error $\hat{\sigma}^2$ (related to random noise) is calculated from equation 8, with $\hat{\mathbf{m}}$ obtained by minimizing the negative log likelihood function over $\mathbf{m}$ via adaptive simplex simulated annealing (Dosso et al., 2001). The covariance matrix $\mathbf{C_D}$ is then used in the Gibbs' sampling procedure of the Bayesian inversion.

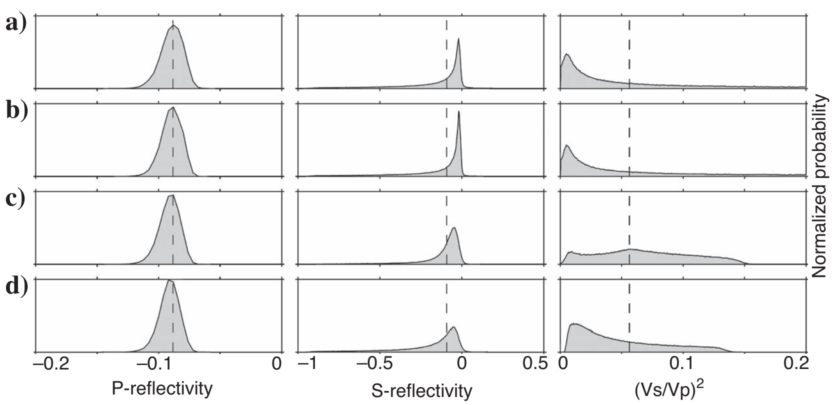

Figure 6. MPDs of parameter combinations from synthetic cases 2a–d, normalized so that the area of each distribution is unity. Dashed lines indicate the true parameter values. (a) Case 2a, with no additional prior information; (b) case 2b, with prior constraints on density; (c) case 2c, with prior constraints on density and the Vp_1–Vs_1 relation; and (d) case 2d, with prior constraints on density, the Vp_1–Vs_1 relation, and P-wave velocity.

Table 4. True model physical parameters for a 15% gas hydrate/1% free-gas model and prior bounds for cases 2a-d. The constraint added to the subsequent case is shown in bold.

Parameter	Vp_1 (m/s)	Vs_1 (m/s)	ρ_1 (kg/m^3)	Vp_2 (m/s)	Vs_2 (m/s)	ρ_2 (kg/m^3)
True value	1768	421	1800	1481	350	1850
Case 2a	-	-	-	-	-	-
Bounds	1000–3000	10–2000	1000–2500	10–3000	10–2000	1000–2500
Case 2b	-	-	-	-	-	-
Bounds	1000–3000	10–2000	**1800 ± 100**	10–3000	10–2000	**1850 ± 100**
Other	$\boldsymbol{\rho_1 \leq \rho_2}$					
Case 2c	-	-	-	-	-	-
Bounds	1000–3000	10–2000	1800 ± 100	10–3000	10–2000	1850 ± 100
Other	$\mathbf{Vs_1[m/s] = (0.4004Vp_1 - 291.9) \pm 200}$; $\rho_1 \leq \rho_2$					
Case2d	-	-	-	-	-	-
Bounds	**1768 ± 150**	10–2000	1800 ± 100	**1481 ± 200**	10–2000	1850 ± 100
Other	Vs_1[m/s] = (0.4004Vp_1 − 291.9) ± 200; $\rho_1 \leq \rho_2$					

Inversion results

To invert the processed AVO data, all the prior information used in case 2d is applied because it was the best-constrained synthetic case. Constraints on the density and the Vp_1–Vs_1 relationship are used, and uniform prior bounds for Vp_1 and Vp_2 are chosen based on NMO velocities for the upper and lower medium, estimated at 1795 ± 150 m/s and 1494 ± 200 m/s, respectively. Inversion results (Figure 10) are slightly less well constrained than for synthetic case 2d, which is explained by the narrower angular range in the measured data. Inversion results obtained without accounting for uncertainty in the seafloor AVO gave a slightly more negative P-wave reflectivity estimate (an average difference of −0.03), and had little effect on S-wave reflectivity results. Although the true answer, of course, is unknown, the use of a full data covariance matrix represents a more realistic treatment of data uncertainties.

As in case 2d, the only parameters that are not well constrained from prior information are Vs_1 and Vs_2, but individual parameter MPDs (Figure 10a) show that the data do not usefully constrain them. Even though the MPD of Vs_1 peaks at 385 m/s (10% gas hydrate concentration based on the rock physics model), the 90% credibility interval for Vs_1 calculated from the MPD is 300–520 m/s (0%–30% gas hydrate concentration). The limited S-wave velocity information is also apparent in the joint MPD of S- versus P-wave reflectivity (Figure 10b), where the S-wave reflectivity is particularly poorly constrained. The intersection of the joint MPD of S- versus P-wave reflectivity with the grid of gas hydrate and free-gas concentrations provides a quantitative estimate of the range of scenarios that satisfy the AVO data. The contour plot indicates that at a 90% credibility level, gas hydrate and free-gas concentrations immediately above and below the BSR are only constrained to be 0%–23% and 0%–2%, respectively. The measured negative reflection coefficients require that there be either some amount of gas hydrate or free gas.

To understand why AVO does not provide adequate constraints on gas hydrate and free-gas concentrations, the relationships between P- and S-wave reflectivity, and gas hydrate and free-gas concentrations must be examined in more detail. Figure 10b shows that the P-wave reflectivity is well constrained by the inversion (between −0.09 and −0.05, at a 90% credibility level). However, even if it were perfectly constrained, P-wave reflectivity would not provide a unique solution for gas hydrate or free-gas concentration. For example, for P-reflectivity of −0.10, the gas hydrate concentration can range from 0%–25%, and free gas, from 0%–3%. This is because the P-reflectivity is a measure of change in P-wave velocity across the BSR, which can be caused by either gas hydrate above, or free gas below, or (most likely) some combination of the two (note that the 0% free-gas case can be excluded if VSP, sonic log, or NMO velocities show clear P-wave velocity reduction relative to the no-gas reference velocity below the BSR). Furthermore, the constraints on P-reflectivity obtained from the AVO inversion could have simply been determined from the near-offset reflection coefficients, without the use of AVO.

Because the S-wave velocity in the lower medium does not change significantly with varying free-gas concentration, the S-wave reflectivity is insensitive to free-gas occurrence. The grid in Figure 10b shows that, if the free-gas concentration is varied while

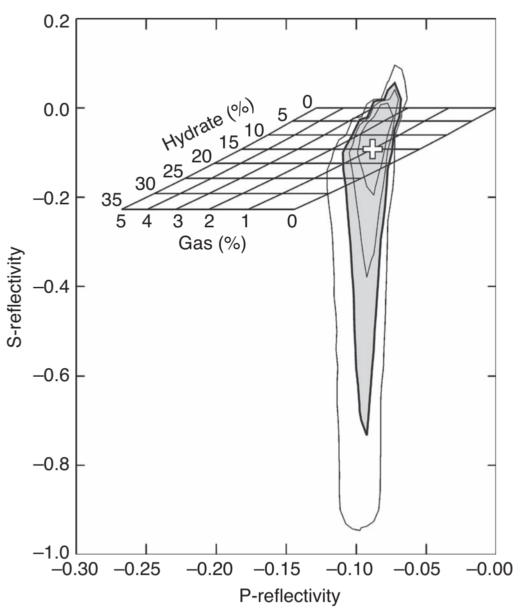

Figure 7. Joint MPDs of S- versus P-wave reflectivity for synthetic case 2d, with prior constraints on density, the Vp_1–Vs_1 relation, and P-wave velocity. The distribution is shown as a contour plot with the 90% credibility contour shaded in. From outermost to innermost, the contours represent 99%, 90%, 75%, and 50% credibility intervals. Contours are overlain with a grid showing where models with varying gas hydrate/free-gas concentration scenarios lie in S- versus P-wave reflectivity space. True model parameter values are indicated by the white cross. Grid nodes falling within the shaded contour represent gas hydrate/free-gas concentration scenarios that could have produced these AVO data at a 90% credibility level.

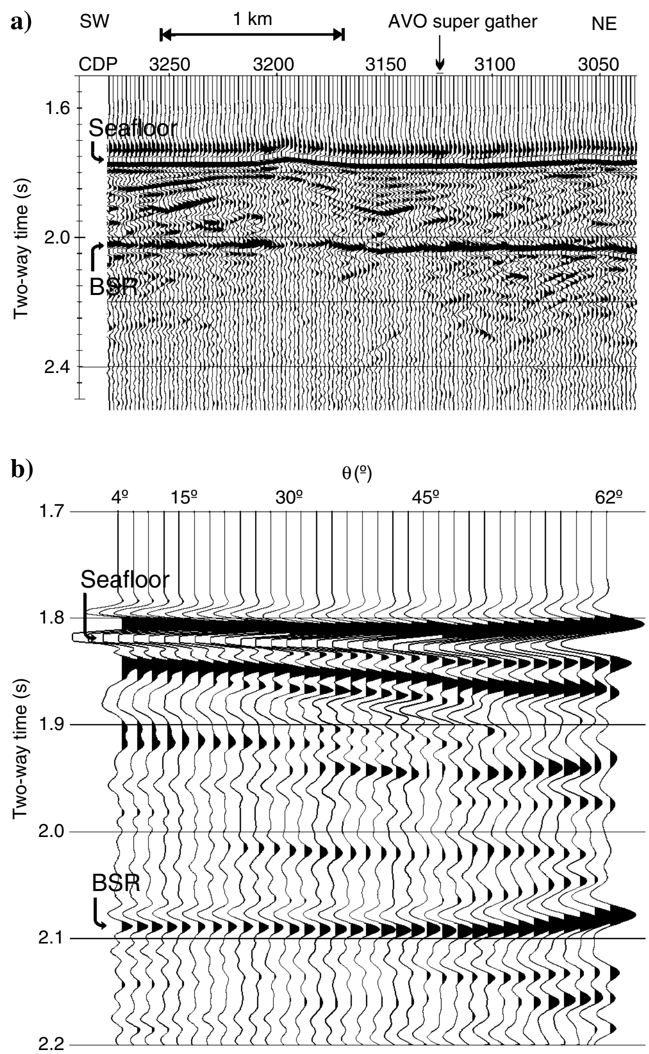

Figure 8. (a) Stacked seismic section of the area of interest, and (b) super CDP gather of traces used in the inversion, where θ is the BSR incidence angle.

holding gas hydrate concentration fixed, S-wave reflectivity remains constant. A unique dependence of S-wave reflectivity on gas hydrate concentration is therefore implied by the rock physics model (at fixed porosity and mineralogy). The grid in Figure 10b shows that an increase in gas hydrate concentration of 5% will cause a decrease in S-wave reflectivity of ~0.03, illustrating that good S-wave reflectivity resolution would provide valuable constraints on gas hydrate concentration. However, Figure 10b clearly shows that the AVO data do not provide nearly enough S-wave reflectivity resolution to constrain gas hydrate concentration. Because the data do not usefully constrain S-wave velocity or S-wave reflectivity, the analysis shows that the AVO method in gas hydrate studies provides no additional information to the analysis of near-offset reflection coefficients or NMO velocity analysis in determining gas hydrate and free-gas concentrations.

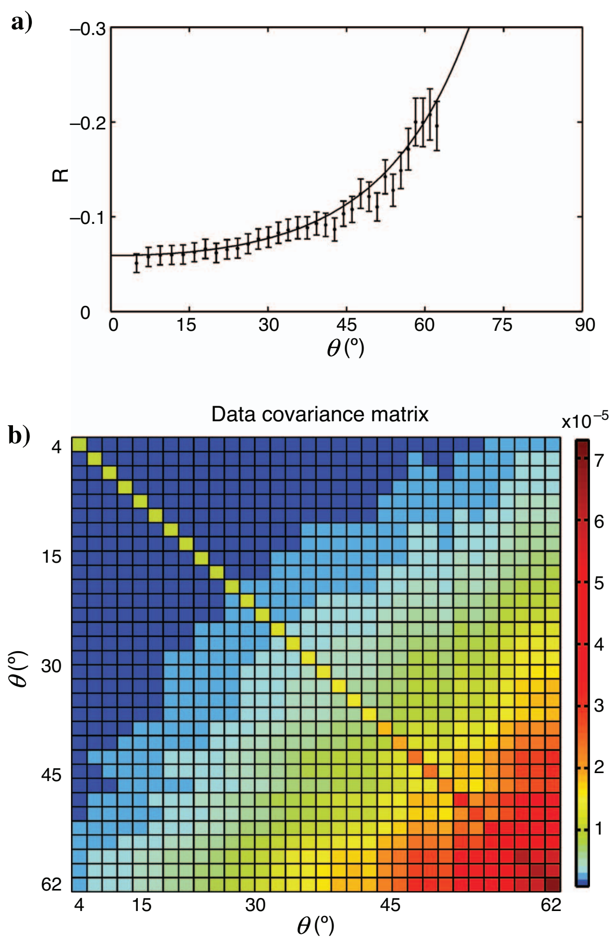

Figure 9. (a) BSR AVO data from MCS line 89-08, CDPs 3123-1326, near IODP site U1327. Reflection coefficients are derived from true-amplitude processed data, and angles are BSR incidence angles obtained from ray tracing. One-standard-deviation error bars are the square root of the corresponding diagonal element of the data covariance matrix. The solid line is the predicted AVO for maximum-likelihood model parameter estimates. (b) Data covariance matrix including both correlated and random error components. Rows and columns of matrix correspond to the AVO data points shown in (a). The colorbar scale is the covariance of reflection coefficients.

OSTRANDER GAS-SAND MODEL

The poor constraint provided by AVO in gas hydrate BSR studies prompts the question of the usefulness of this tool for other geophysical problems, such detecting oil and gas. To address this question, the Bayesian AVO inversion is applied to reflections from the top of the sand layer in the now-classic Ostrander (1984) gas-sand model (a low velocity gas-charged sandstone layer between high-velocity shale layers). Physical parameters for each layer given by Ostrander (1984) are summarized in Table 5. A major difference between Ostrander's gas-sand model and the gas hydrate models is that the gas-sand model represents consolidated sediments, with greater values for Vp, Vs, and ρ. As in the gas hydrate case, gas in the sand unit reduces Vp. However, the upper unit in Ostrander's model has reduced Vs for typical shale beds. Probabilistic AVO inversion is commonly

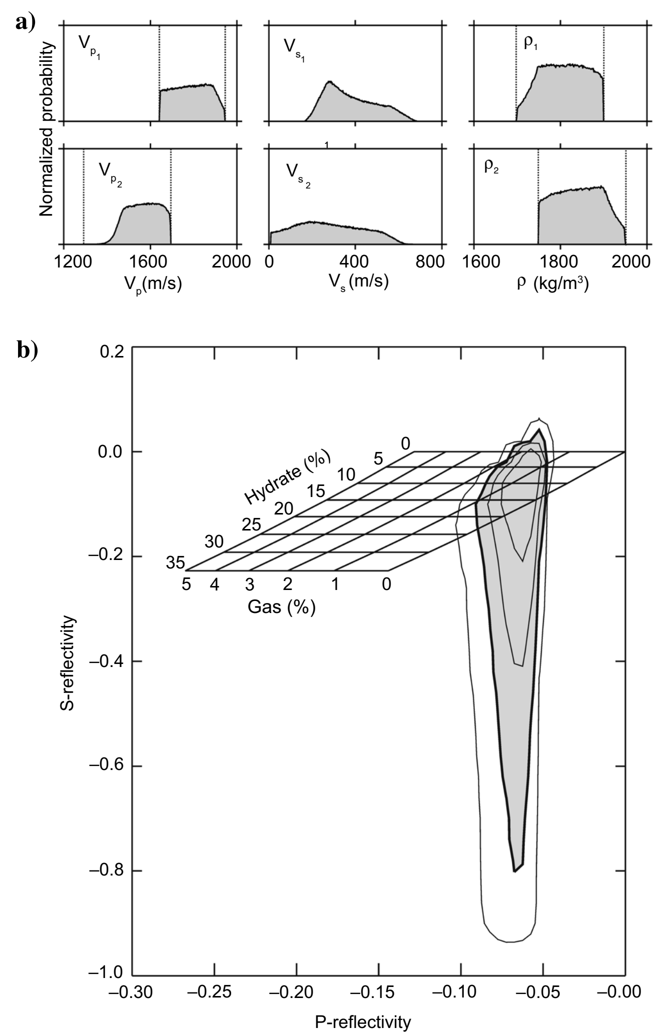

Figure 10. Parameter MPDs of inverted AVO data. (a) MPDs of individual parameters with dotted lines indicating the prior bounds used in the inversion. (b) Joint MPD of S- versus P-wave reflectivity shown as a contour plot with the 90% credibility contour shaded in. From outermost to innermost, the contours represent 99%, 90%, 75%, and 50% credibility intervals. Contours are overlain with a grid showing where models with varying gas hydrate/free-gas concentration scenarios lie in S- versus P-wave reflectivity space. Grid nodes falling within the shaded contour represent gas hydrate/free-gas concentration scenarios that could have produced these AVO data at a 90% credibility level.

used in oil and gas type problems (Drufuca and Mazzotti, 1995; Avseth et al., 2001; Buland and Omre, 2003; Mazotti and Zamboni, 2003; Hampson et al., 2004) to provide quantitative estimates of lithology, porosity, and/or pore-space saturation. This part of the study applies the gas hydrate AVO procedure to gas-sands to determine how well AVO can detect the presence of gas in the sand unit.

Synthetic AVO data generated from Ostrander's model using the Zoeppritz equations are shown in Figure 11. The angular range is 0°–80°, and Gaussian-distributed random errors with 0.01 standard deviation are included. The synthetic AVO data are inverted using the same Bayesian approach. As prior information, the densities of both media are constrained by well-log data, and Vp_1 and Vs_1 (in the shale) are related by the Castagna et al. (1985) mudrock relation. This equation is reordered to accept a reasonable range of Vs_1 values for a given Vp_1:

$$Vs_1 = (0.862Vp_1 - 1172) \pm 400. \qquad (12)$$

True model parameters and prior constraints are summarized in Table 5.

Inversion results are shown as joint MPDs of model parameters in Figure 12. Of interest is the observed correlation between Vp_2 and Vs_2 (Figure 12d), because the relationship between these parameters is affected by the presence of gas. Castagna et al. (1985) showed that water-saturated sandstones and shales plot along the mudrock line in Vp−Vs space. Smith and Gidlow (1987) and Fatti et al. (1994) further showed that gas-charged sandstones are displaced from the mudrock line, with reduced Vp for a given Vs. Physically, this occurs because the presence of gas in the sand reduces P-wave velocities, but has little or no effect on S-wave velocities (Gregory, 1976). This effect is clearly observed in the joint MPD of Vs_2 versus Vp_2 (Figure 12d), as the distribution is separated from the mudrock line, qualitatively indicating that the sand is gas-charged. For quantitative estimates and uncertainties of porosity, an appropriate rock physics model is needed (e.g., Gassmann, 1951).

The successful application of the AVO inversion scheme to Ostrander's gas-sand model and its failure for gas hydrate BSRs demonstrates that the usefulness of AVO depends on the physical properties of the material in question. AVO inversion for the gas-sand model resolves a relationship between Vp_2 and Vs_2, which allows gas-saturated sandstones to be distinguished from wet sandstones.

SUMMARY AND DISCUSSION

This paper examines the applicability of AVO in determining gas hydrate and free-gas concentrations above and below a BSR interface. The synthetic AVO analysis for gas hydrate BSRs indicates that it is not possible to resolve all physical parameters (Vp_1, Vs_1, ρ_1, Vp_2, Vs_2, and ρ_2) at the BSR interface using MCS data. The study suggests that the most important factors affecting the AVO uncertainty are prior knowledge of the properties of the upper media and the angular range of the data.

Useful constraints on gas hydrate and free-gas concentrations at the BSR interface do not require all parameters be individually constrained; information about interparameter relationships can be diagnostic. The inversion shows that P-wave reflectivity is the best-resolved parameter, followed by S-wave reflectivity, with little infor-

Table 5. True model physical parameters for Ostrander's gas-sand model and prior bounds for the inversion.

Parameter	Vp_1 (m/s)	Vs_1 (m/s)	ρ_1 (kg/m^3)	Vp_2 (m/s)	Vs_2 (m/s)	ρ_2 (kg/m^3)
True value	3048	1244	2400	2438	1626	2140
Bounds	10–5000	10–3000	2400 ± 100	10–5000	10–3000	2140 ± 100
Other	$Vs_1(m/s) = (0.862Vp_1 - 1172) \pm 400$					

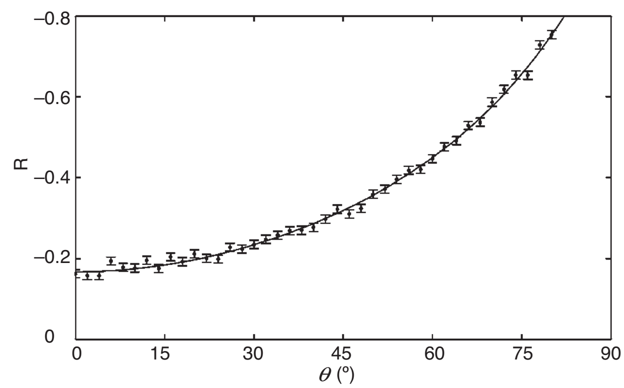

Figure 11. Synthetic AVO data generated from reflections off the top of the Ostrander gas-sand model. Random Gaussian noise with σ = 0.01 is added to the data. One-standard-deviation error bars are shown and the solid line is the error-free AVO curve.

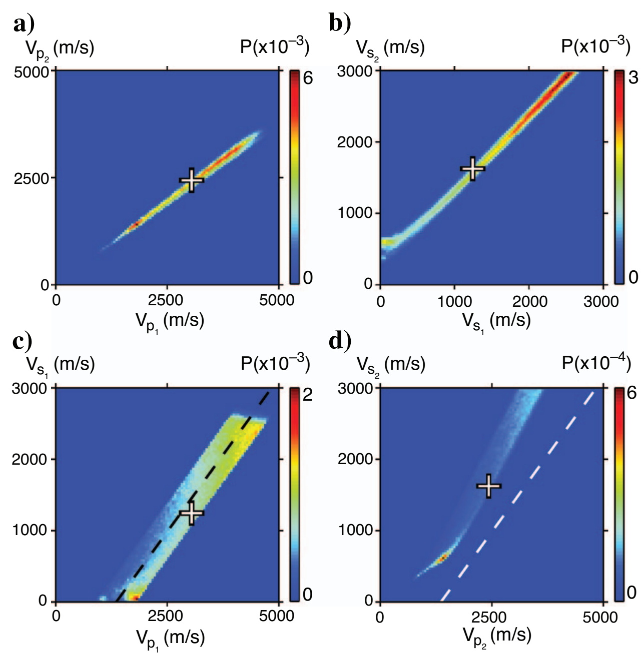

Figure 12. Joint MPDs of selected parameters from Ostrander's gas-sand model. The colorbar scale is normalized probability (P), and the crosses indicate true parameter values. (a) shows Vp_2 versus Vp_1, (b) shows Vs_2 versus Vs_1, (c) shows Vs_1 versus Vp_1 (in the shale), and (d) shows Vs_2 versus Vp_2 (in the gas-sand). In (c) and (d), the dashed line is the mudrock line, indicating the expected Vp-Vs trend for shales and water-saturated sandstones.

mation about the $Vp-Vs$ relationship. From a physical point of view, parameters such as P- and S-wave reflectivity (which depend on properties of both media) are best resolved because of the nature of the data: Measured seismic reflections occur because of changes in physical properties across an impedance boundary. The lack of information content of the data with respect to the $Vp-Vs$ relationship in either medium greatly limits independent determination of gas hydrate and free-gas concentrations.

Inversion of AVO data from offshore Vancouver Island is interpreted as a joint MPD of P- and S-wave reflectivity, overlain with a grid of P- and S-wave reflectivity values for different gas hydrate/free-gas concentration scenarios, determined from a rock physics model. This approach provides a means to interpret parameter MPDs in terms of gas hydrate and free-gas concentration estimates. At a 90% credibility level, gas hydrate and free-gas concentrations at the study location are poorly constrained, i.e., 0%–23% and 0%–2% immediately above and below the BSR. Furthermore, synthetic cases that used larger angular ranges and included smaller data errors gave a similar degree of constraint, demonstrating that an improvement in data quality or angular range does not improve the results significantly.

The joint MPD of P- and S-wave reflectivity shows the range of gas hydrate/free-gas-concentration scenarios that satisfy both the data and the prior information included in the inversion. The distribution is poorly constrained because of poor S-wave reflectivity resolution, which can be understood by examining the rock physics model. According to the gas hydrate in-frame model used, where gas hydrate is a load-bearing component of the sediment matrix, Vs for a medium with 15% gas hydrate concentration is 421 m/s, whereas Vs for a medium with 1% free-gas is 350 m/s — a change of only 71 m/s. This degree of resolution cannot be expected from marine MCS data, where only P-waves are measured directly and Vs information is obtained indirectly through Vp information and AVO because uncertainties in Vp are estimated to be at least ± 100 m/s. As for P-wave velocity and density information, the inversion does not constrain their values any more than the prior information, indicating that AVO is not a useful way to obtain information about these parameters. The most reliable method to obtain P-wave velocity information is NMO velocity analysis, whereas BSR P-wave reflectivity information is obtained most easily from near-vertical incidence BSR reflection coefficients.

The lack of success of AVO in this and other gas hydrate studies can be attributed to the fact that the BSR represents only a relatively small contrast in physical properties, and that BSRs studied here occur in unconsolidated sediments of $\sim 50\%$ porosity, with low S-wave velocities. Fundamentally, AVO is an indirect method of obtaining S-wave information, which is not sensitive enough to be useful in unconsolidated sediments. An alternative approach is the use of ocean-bottom receivers that directly measure the shear wavefield via P-S mode-converted waves (Stewart et al., 2002; Andreassen et al., 2003).

AVO inversion of synthetic data generated from Ostrander's gas-sand model shows that the success of AVO depends on the properties of the sediment sections. In this case, inversion results show a strong relationship between S- and P-wave velocities in the sandstone unit, with values of these parameters diagnostically indicative of gas-charged sandstones. The improvement in inversion resolution for the gas-sand case over the gas hydrate cases is attributed to the fact that, in the gas-sand case, (1) the formations are consolidated sediments with greater P- and S-wave velocities, allowing the relationship between Vp and Vs to be further constrained; (2) the contrast in physical properties at the boundary is greater because it is a lithologic boundary (as opposed to a change in pore-space saturation, as in the gas hydrate case), leading to a more diagnostic AVO curve and more resolvable P- and S-wave velocity contrasts; and (3) because, in Ostrander's model, where only properties of the sandstone unit are sought, the problem has fewer degrees of freedom than the gas hydrate case, where both gas hydrate and free-gas concentrations are unknown.

The variable degree of success obtained in this AVO study highlights the need to include rigorous quantitative uncertainties in all AVO studies. The appeal of the Bayesian approach to inverting AVO data is that the results are accompanied by realistic quantitative error estimates, allowing the interpreter to accurately gauge the reliability of results.

ACKNOWLEDGMENTS

We thank George Spence, Ross Haacke, and Patrick Hart whose insightful reviews greatly improved an earlier version of the manuscript. We also thank Andrew Calvert for providing the archived MCS data. Fellowship funding for MPC was provided by the Natural Sciences and Engineering Research Council of Canada (NSERC). Research support was provided by NSERC and the Geological Survey of Canada (publication no. 20060084).

REFERENCES

Andreassen, K., K. A. Berteussen, H. Sognnes, K. Henneberg, J. Langhammer, and J. Mienert, 2003, Multicomponent ocean bottom cable data in gas hydrate investigation offshore Norway: Journal of Geophysical Research, **108**, 2399.

Andreassen, K., P. Hart, and A. Grantz, 1995, Seismic studies of a bottom simulating reflection related to gas hydrate beneath the continental margin of the Beaufort Sea: Journal of Geophysical Research, **100**, 12,659–12,673.

Andreassen, K., P. E. Hart, and M. MacKay, 1997, Amplitude versus offset modeling of the bottom simulating reflection associated with submarine gas hydrates: Marine Geology, **137**, 25–40.

Avseth, P., T. Mukerji, A. Jorstad, G. Mavko, and T. Veggerland, 2001, Seismic reservoir mapping from 3-D AVO in a North Sea turbidite system: Geophysics, **66**, 1157–1176.

Buland, A., and H. Omre, 2003, Bayesian linearized AVO inversion: Geophysics, **68**, 185–198.

Castagna, J. P., M. L. Batzle, and R. L. Eastwood, 1985, Relationships between compressional-wave and shear-wave velocities in clastic silicate rocks: Geophysics, **50**, 571–581.

Collett, T. S., M. Riedel, and Expedition 311 Scientists, 2005, Cascadia margin gas hydrates: IODP Preliminary Report, **311**, http://dx.doi.org/10.2204/iodp.pr.311.2005.

Dosso, S. E., 2002, Quantifying uncertainties in geoacoustic inversion I: A fast Gibbs sampler approach: Journal of the Acoustical Society of America, **111**, 129–142.

Dosso, S. E., M. J. Wilmut, and A. L. Lapinski, 2001, An adaptive hybrid algorithm for geoacoustic inversion: IEEE Journal of Oceanic Engineering, **26**, 324–336.

Drufuca, G., and A. Mazzotti, 1995, Ambiguities in AVO inversion of reflections from gas-sand: Geophysics, **60**, 134–141.

Duren, R. E., 1991, Seismic range equation: Geophysics, **56**, 1015–1026.

Dvorkin, J., and A. Nur, 1993, Rock physics for characterization of gas hydrates, *in* The future of energy gases: U. S. Geological Survey Professional Paper 1570.

Ecker, C., J. Dvorkin, and A. Nur, 1998, Sediments with gas hydrates: Internal structure from seismic AVO: Geophysics, **68**, 1659–1669.

Fatti, J. L., G. C. Smith, P. J. Vail, P. J. Strauss, and P. R. Levitt, 1994, Detection of gas in sandstone reservoirs using AVO analysis: A 3-D seismic case history using the Geostack technique: Geophysics, **59**, 1362–1376.

Gassmann, F., 1951, On elasticity of porous media: Vierteljahresschrift der Naturforschenden Gesellschaft Zurich, **96**, 1–13.

Gregory, A. R., 1976, Fluid saturation effects on dynamic elastic properties of sedimentary rocks: Geophysics, **41**, 895–921.

Hamilton, E. L., 1976, Variations of density and porosity with depth in deep-sea sediments: Journal of Sedimentary Petrology, **46**, 280–300.
Hampson, D., B. Russell, and M. Cardamone, 2004, Uncertainty in AVO – How can we measure it?: CSEG Recorder, **29**, 5–11.
Helgerud, M. B., 2001, Wave speeds in gas hydrate and sediments containing gas hydrate: A laboratory and modeling study: Ph.D. thesis, Stanford University.
Hyndman, R. D., and G. D. Spence, 1992, A seismic study of methane hydrate bottom simulating reflectors: Journal of Geophysical Research, **97**, 6683–6698.
Kvenvolden, K. A., G. D. Ginsburgh, and V. A. Soloviev, 1993, Worldwide distribution of subaquatic gas hydrates: Geo-Marine Letters, **13**, 32–40.
Mazotti, A., and E. Zamboni, 2003, Petrophysical inversion of AVA data: Geophysical Prospecting, **51**, 517–530.
Ostrander, W. J., 1984, Plane-wave reflection coefficients for gas sands at nonnormal angles of incidence: Geophysics, **49**, 1637–1648.
Riedel, M., S. E. Dosso, and L. Beran, 2003, Uncertainty estimation for amplitude variation with offset (AVO) inversion: Geophysics, **68**, 1485–1496.
Sen, M. K., and P. L. Stoffa, 1996, Bayesian inference, Gibbs' sampler and uncertainty estimation in geophysical inversion: Geophysical Prospecting, **44**, 313–350.
Sheriff, R. E., and L. P. Geldart, 1982, Exploration seismology: History, theory, data acquisition vol. 1: Cambridge University Press.
Smith, G. C., and P. M. Gidlow, 1987, Weighted stacking for rock property estimation and detection of gas: Geophysical Prospecting, **35**, 993–1014.
Spence, G. D., R. D. Hyndman, E. E. Davis, and C. J. Yorath, 1991a, Marine multichannel seismic reflection data across the continental margin of Vancouver Island: Geological Survey of Canada Open File Report 2391.
———, 1991b, Seismic structure of the northern Cascadia accretionary prism: Evidence from new multichannel seismic reflection data, *in* R. Meissner, L. Brown, H.-J. Durbaum, W. Franks, K. Fuchs, and F. Seifert, eds., Continental lithosphere: Deep seismic reflections: American Geophysical Union Geodynamics Series, **22**, 257–263.
Stewart, R. R., J. E. Gaiser, R. J. Brown, and D. C. Lawton, 2002, Converted wave seismic exploration: Methods: Geophysics, **67**, 1348–1363.
Tarantola, A., 1987, Inverse problem theory: Methods for data fitting and model parameter estimation: Elsevier Science Publ. Co., Inc.
Tréhu, A. M., G. Bohrmann, F. Rack, M. E. Torres, and Leg 204 Scientific Party, 2003, Proceedings of the Ocean Drilling Program: Initial Reports, **204**, http://www-odp.tamu.edu/publications/204_IR/204ir.html, accessed April 7, 2006.
Westbrook, G. K., B. Carson, R. Musgrave, and Shipboard Scientific Party, 1993, Proceedings of the Ocean Drilling Program: Initial Reports, 146, p. 1: ODP Publication Services.
Wood, W. T., W. S. Holbrook, and H. Hoskins, 2000, In situ measurements of P-wave attenuation in the methane hydrate- and gas-bearing sediments of the Blake Ridge, *in* C. K. Paull, R. Matsumoto, P. J. Wallace, and W. P. Dillon, eds., Scientific results: Proceedings of the Ocean Drilling Program, **164**, 365–272.
Yuan, T., R. D. Hyndman, G. D. Spence, and B. Desmons, 1996, Velocity structure of a bottom-simulating reflector and deep sea gas hydrate concentrations on the Cascadia continental slope: Journal of Geophysical Research, **101**, 13655–13671.
Yuan, T., G. D. Spence, and R. D. Hyndman, 1994, Seismic velocities and inferred porosities in the accretionary wedge sediments at the Cascadia margin: Journal of Geophysical Research, **99**, 4413-4427.
Yuan, T., G. D. Spence, R. D. Hyndman, T. A. Minshull, and S. C. Singh, 1999, Seismic velocity studies of a gas hydrate bottom-simulating reflector on the northern Cascadia continental margin: Amplitude modeling and full waveform inversion: Journal of Geophysical Research, **104**, 1179–1191.
Zoeppritz, R., 1919, On the reflection and propagation of seismic waves: Erdbebenwellen VIIIB; Göttinger Nachrichten, I, 66–84.